Ultramicroscopy 247 (2023) 113700

Contents lists available at ScienceDirect

Ultramicroscopy

journal homepage: www.elsevier.com/locate/ultramic

A reference-area-free strain mapping method using precession electron diffraction data

Dexin Zhao [a,1], Aniket Patel [a,1], Aaron Barbosa [a], Marcus H. Hansen [a], Ainiu L. Wang [a], Jiaqi Dong [a], Yuwei Zhang [b], Tejas Umale [a], Ibrahim Karaman [a], Patrick Shamberger [a], Sarbajit Banerjee [c], Matt Pharr [b], Kelvin Y. Xie [a,*]

[a] *Department of Materials Science and Engineering, Texas A&M University, College Station, TX 77843, USA*
[b] *Department of Mechanical Engineering, Texas A&M University, College Station, TX 77843, USA*
[c] *Department of Chemistry, Texas A&M University, College Station, TX 77843, USA*

ARTICLE INFO

Keywords:
Strain mapping
Precession electron diffraction (PED)
Denoise
VO_2
Shape memory alloys (SMA)

ABSTRACT

In this work, we developed a method using precession electron diffraction data to map the residual elastic strain at the nano-scale. The diffraction pattern of each pixel was first collected and denoised. Template matching was then applied using the center spot as the mask to identify the positions of the diffraction disks. Statistics of distances between the selected diffracted disks enable the user to make an informed decision on the reference and to generate strain maps. Strain mapping on an unstrained single crystal sapphire shows the standard deviation of strain measurement is 0.5%. With this method, we were able to successfully measure and map the residual elastic strain in VO_2 on sapphire and martensite in a $Ni_{50.3}Ti_{29.7}Hf_{20}$ shape memory alloy. This approach does not require the user to select a "strain-free area" as a reference and can work on datasets even with the crystals oriented away from zone axes. This method is expected to provide a robust and more accessible alternative means of studying the residual strain of various material systems that complements the existing algorithms for strain mapping.

1. Introduction

Stored elastic strain has a profound impact on the mechanical properties and functionalities of materials. For example, compressive residual stresses in metals and ceramics can suppress crack propagation, thereby improving the fracture toughness [1,2]. Residual elastic strain can also affect band gaps, electron transport, and phonon transport [3–5]. X-ray diffraction and neutron diffraction are two popular techniques to measure and map the residual strain in materials [6,7]. Since both x-ray and neutron beams are difficult to focus, the residual strain mapping using these two techniques has limited spatial resolution.

To achieve nanometer-scale resolution strain mapping, transmission electron microscopy (TEM) and electron diffraction have been employed. Electrons are charged particles, and thus electron beam can be focused by tuning the strength of the electromagnetic lenses in TEM. The elastic strain can be calculated from high-resolution TEM (HRTEM) micrographs in real space or by analyzing diffraction pattern information in reciprocal space [8,9]. For the real-space imaging mode, geometric phase analysis (GPA) is widely used [10,11]. Although quite powerful, GPA can only be used on HRTEM micrographs, in which the phase contrast is dominant; it cannot be applied on regular bright-field (BF) TEM images, where lattice fringes are absent. Hence, GPA has high spatial resolution but a limited field of view (typically less than or approximately 20×20 nm^2).

In diffraction mode, Zuo and Spence pioneered the work using convergent-beam electron diffraction (CBED) to obtain the strain information and automate the process [12,13]. In the CBED patterns, lattice strain can be precisely measured by tracking the positions of higher-order Laue zone (HOLZ) lines in the bright-field CBED disk [14,15]. This approach works because HOLZ lines result from high-order reflections, which are very sensitive to changes in the lattice spacing [9]. By comparing the experimentally acquired HOLZ line positions to computer simulations, strain information with high precision (approximately 0.2%) can be obtained [16,17].

---

* Corresponding author.
E-mail address: kelvin.xie@tamu.edu (K.Y. Xie).
[1] These authors contributed equally to this work.

https://doi.org/10.1016/j.ultramic.2023.113700
Received 25 July 2022; Received in revised form 29 October 2022; Accepted 4 February 2023

With the advent of 4D-STEM [18,19] and precession electron diffraction (PED) [20,21], a more computationally cost-effective way to perform strain mapping is to raster the beam on the specimen, acquire the diffraction pattern at each pixel, and measure the shifts of diffraction spots for each pixel relative to a reference pattern. PED combines beam precession (the beam is tilted and rotated about the optical axis at a very high frequency, typically 100 Hz) with nanobeam diffraction and offers a number of advantages in performing strain mapping compared to 4D-STEM. First, PED averages out the dynamical effects in electron diffraction, leading to more uniform diffraction spot intensity and easier spot center identification [22,23]. In contrast, 4D-STEM utilizes CBED patterns, and the illumination in the diffraction disks is non-uniform; the disk center identification usually involves the use of specially patterned apertures or additional reconstruction steps [24–28]. Second, PED excites higher-order reflections, which are more sensitive to changes in lattice parameter [8].

The current strain mapping methods used by 4D-STEM and PED share very similar algorithms [29,30]. The specimen is tilted to a low-index zone, and a “strain-free” reference pattern is acquired. Two non-collinear diffraction spots are then selected to create the two non-collinear vectors, g_1 and g_2. The coordinates of the two vectors in the reference diffraction can be expressed as the reference diffraction matrix $G_0 = (g_{x1}\ g_{x2}\ g_{y1}\ g_{y2}\ )$. The two vectors in the diffraction pattern for strain calculation can be expressed in the same way as the diffraction matrix G. The distortion matrix D hence can be simply expressed as $D = (G_0G^{-1})^t$, where t is the transpose of the matrix. The distortion matrix can be further decomposed into a pure deformation matrix and rotation matrix to generate information of ε_{xx}, ε_{yy}, ε_{xy}, and the rotation angle θ to generate strain maps at nanometer and submicron scale from both 4D-STEM and PED datasets [24,29,31–37].

We realize two features of the above algorithm may limit its wider application of strain mapping. First, a reference area is required. In many cases, it is difficult to identify the appropriate “strain-free” diffraction pattern, and its selection can be user-dependent and lacking the support of quantitative data. This shortcoming is particularly important in materials that contain high density of dislocations (e.g., martensite grains or heavily deformed grains) and nanocrystalline samples, in which an un-strained pristine area is difficult to find. Second, the algorithm requires the sample to be tilted to a low-index zone axis so that two non-colinear vectors can be drawn. If the sample is at a two-beam condition, the above algorithm would fail to work. In this light, we developed a new PED-based strain mapping algorithm that does not rely on the selection of the reference diffraction pattern and can also work even when the sample is not tilted to a low-index zone axis.

2. Materials and methods

Diffraction patterns were obtained with a 200 kV *FEI Tecnai F20 ST* TEM equipped with a field emission gun. A *NanoMEGAS ASTAR* unit was used to produce precession and descanning of the electron beam. The spot size of the electron beam with a 0.3° precession angle is approximately 3 nm. All diffraction patterns were acquired in the images with 580×580 pixel resolution.

A VO_2 thin film deposited on a *c*-cut single crystal sapphire substrate and a $Ni_{50.3}Ti_{29.7}Hf_{20}$ shape memory alloy (SMA) were used as model materials. The growth of VO_2 on [0001] sapphire is highly epitaxial, and thus residual strain is expected near the interface [38]. The $Ni_{50.3}Ti_{29.7}Hf_{20}$ shape memory alloy is martensitic at room temperature [39], and elastic strain is expected to be stored in the material during the austenite to martensite transformation. VO_2 deposition was achieved by sputtering from a pure V target using a pressure of 2.0 mTorr with a mixture of argon and oxygen gas (Ar: 20 sccm, O_2: 4.1 sccm) and a DC power of 200 W at 600 °C for 30 min then annealed in the chamber for another 30 min. Cross-sectional TEM specimens were prepared using a Thermo-Fisher Helios G4 focused-ion beam (FIB). The $Ni_{50.3}Ti_{29.7}Hf_{20}$ SMA was produced by high vacuum induction melting of high purity Ni, Ti, and Hf. The sample was then solution treated to achieve a precipitate-free microstructure. The TEM specimens were prepared from 3 mm disks and electropolished using a Tenupol-5 polishing system with a solution of 30% nitric acid in ethanol at −40 °C to create electron transparent areas. More detailed microstructural information on the SMA can be found in our earlier work [40].

3. Results and discussion

3.1. Architecture of the algorithm

The strain mapping algorithm was written in Python and consists of five steps. The workflow is shown in Fig. 1. First, it reads the .blo file using HyperSpy [41]. Second, the user can select a filter (Gaussian, non-local means, or Wiener) to denoise the diffraction patterns for each pixel. Third, the center diffraction disk is used as a template to identify the positions of other diffracted beam disks using a correlation coefficient cutoff (0.87 in the default setting). Fourth, the user will select two diffraction disks of interest. The algorithm will go through all diffraction patterns, calculate the distance of the selected disks, and generate a distance histogram. Note the distance is measured in reciprocal space, and the unit is pixel. Finally, the user will determine a “strain-free distance” based on the distance histogram, and the algorithm will create the “strain heat map”.

3.2. Function of each step of the algorithm

In the first step, HyperSpy, which is an open-source multi-dimensional data analysis package, was used to read and open the .blo file (generated by the *NanoMEGAS* PED system) in the *Python* environment [41].

The second step aims to denoise the diffraction patterns, and its importance will be elucidated in the third step shortly. The diffraction pattern shown in Fig. 2 was acquired from a single crystal sapphire tilted to the $[1)\overline{2}10]$ zone axis. In the as-acquired condition, the diffraction patterns are noisy (Fig. 2a), and background can be described as Poisson noise [42]. The fuzzy noise is better revealed by the close-up views of the center disk (red boxed region) and a diffracted disk (blue boxed region). The noise is also illustrated as high-frequency spikes in the corresponding 3D intensity profiles.

One “brute-force” way to improve the signal-to-noise ratio is to increase the acquisition time of the diffraction pattern at each pixel. However, this approach would lead to prolonged acquisition time and

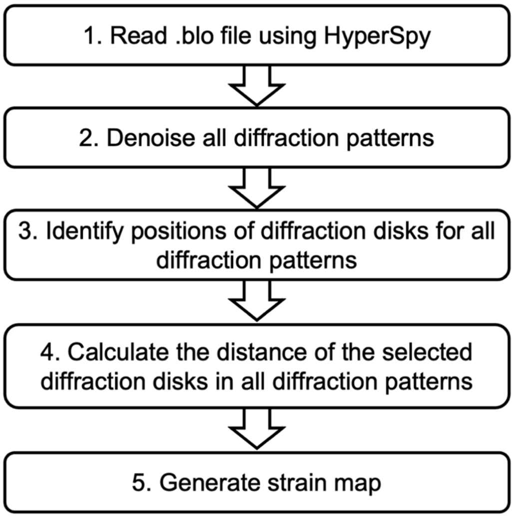

Fig. 1. Flowchart describing the key steps of the strain mapping algorithm.

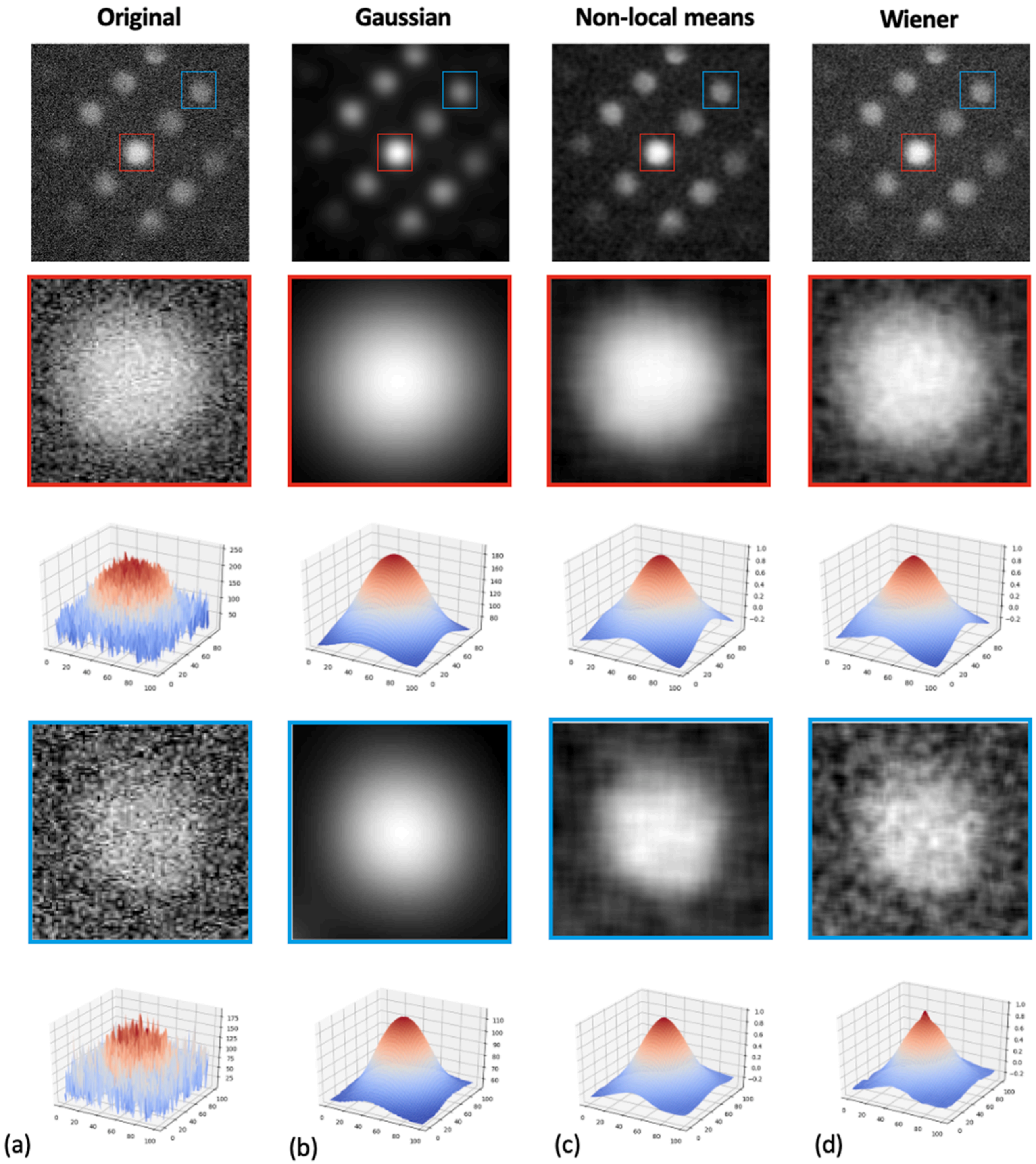

Fig. 2. (a) As-acquired (original), (b) Gaussian filtered, (c) non-local means filtered, and (d) Wiener filtered diffraction pattern from a sapphire single crystal oriented to the $[1\bar{2}10]$ zone axis. The red boxed and blue boxed regions are zoomed-in views of the direct beam and a diffracted disk, respectively. The corresponding 3D intensity profiles are also presented. (For interpretation of the references to color in this figure legend, the reader is referred to the web version of this article.)

may result in damage to beam-sensitive samples. An alternative way to reduce the noise is to apply image filters. Here, three common image filters [24,42] were applied: a Gaussian filter ($\sigma = 1.15$), a non-local means filter ($\sigma = 1.15$, patch size = 3, and patch distance = 6), and a Wiener filter (filter size = 5 and noise power = 5). Note that the fine details of the filters can be tuned by users. The noise level has reduced substantially after applying the filters in all three cases, as shown in Fig. 2b-d. In particular, the 3D intensity plots of the center and diffracted disks exhibit smooth profiles, confirming the success of denoising from the image filters.

In the third step, the center disk was used as the template to identify the position of diffracted disks. In this work, we used a correlation coefficient of 0.87 as the cutoff for template matching [43], and the user can choose a different value. The identified diffraction disk positions are marked by red dots in Fig. 3. In the original unfiltered image (Fig. 3a), only the center spot was identified as itself was used as the template. Disk position identification was drastically improved with the denoise step. Multiple diffracted disks were recognized in the Gaussian filtered

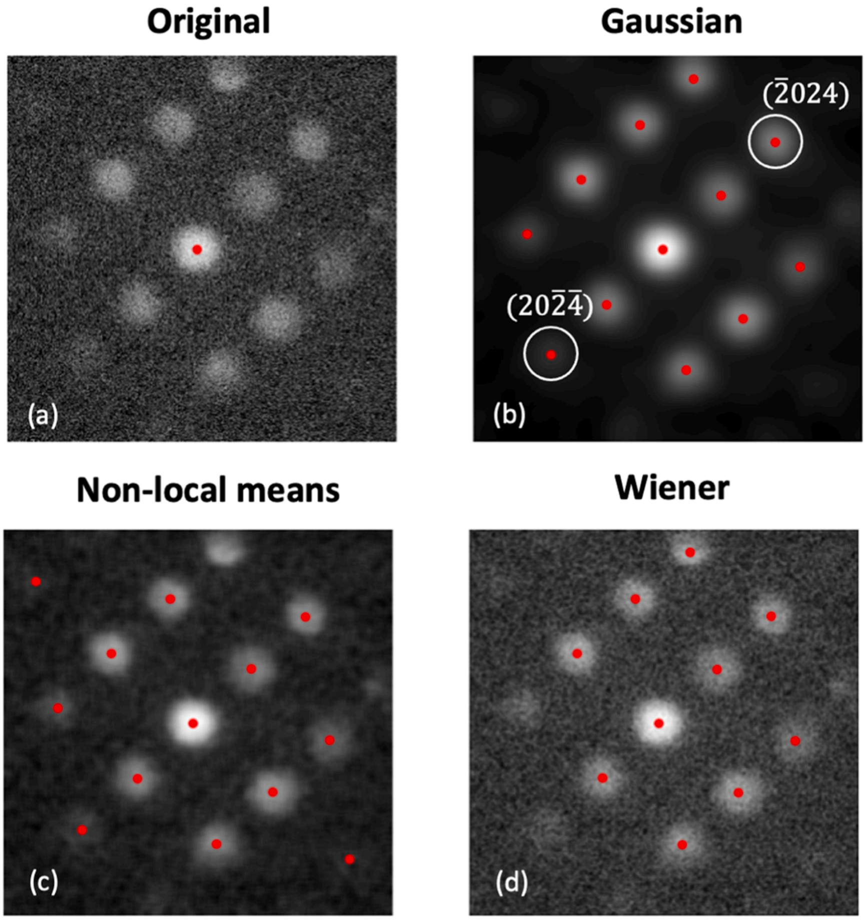

Fig. 3. Diffraction disk position identification using the direct beam as the mask in the (a) original, (b) Gaussian filtered, (c) non-local means filtered, and (d) Wiener filtered diffraction patterns. Red dots indicate the position of identified disks. (For interpretation of the references to color in this figure legend, the reader is referred to the web version of this article.).

(Fig. 3b), non-local mean filtered (Fig. 3c), and Wiener filtered (Fig. 3d) diffraction patterns. Note that in many cases, multiple locations from one diffraction disk can have a correlation coefficient higher than the cutoff. The algorithm only uses the location with the highest correlation coefficient within 30 pixels to preclude duplicate identification of the same diffraction disk. It is also worth noting that the correlation coefficient is only one of the means to determine diffraction disk positions. Other algorithms, such as PixSTEM [44], blob detection [37], and trained neural networks [28], may also be incorporated into the code to locate diffraction disk positions.

In the fourth step, the user will select two diffracted disks. The distance between these two disks is calculated from each pixel in the PED data. Then a distance histogram will be generated, and the distance data are exported as a .csv file. In the example, Fig. 4a displays the distance histogram generated by measuring the distance of the $(20\bar{2}\bar{4})$ disk and the $(\bar{2}024)$ disk (marked by white circles in Fig. 3b) of the Gaussian filtered dataset. The histogram appears to be composed of "peak bundles", which is related to the discretization of the pixel spacing in the underlying diffraction patterns. Since the material is a single crystal of sapphire, there should be no elastic strain stored in the specimen. One can simply consider the mean value of all the measured distances to be the "strain-free distance". Note that there is a spread of data in the distance measurement. Such a spread may be attributed to the slight measurement error from the algorithm and is manifested as noise in the distance map in Fig. 4b. The "mean distance" approach can also be used in materials with symmetric strain distribution (e.g., the tensile and compressive strain fields from the same dislocation core). The appropriateness of using the "mean distance" as the "strain-free distance" in systems with asymmetric strain distribution will be discussed shortly in the first case study.

In the fifth step, a strain map will be generated based on the entered "strain-free distance" and the measured distance from each diffraction pattern. The strain is calculated using the equation

$$\varepsilon = \frac{\frac{1}{d_i} - \frac{1}{d_0}}{\frac{1}{d_0}} = \frac{d_0}{d_i} - 1$$

where d_i is the measured distance and d_0 is the "strain-free distance" entered by the user. The single crystal sapphire example from the previous step can be considered as a baseline. The calculated average strain value is 0 and the standard deviation is 0.5% strain (Fig. 4c,d). Consequently, the probability of a strain-free pixel showing a strain value of 1% and greater (both compressive and tensile) is only 4.6%. Hence, if a region displays strains 1% and greater, the strain is likely to be true.

3.3. *Case study 1: strain associated with a VO2 thin film on a c-cut single crystal sapphire*

In the first case study, a M-phase VO_2 thin film grown on a *c*-cut single crystal sapphire substrate was used as a model system. Fig. 5a shows a virtual dark-field image reconstructed using the intensity of the (0006) diffraction spot in sapphire (highlighted with the dashed circle) in the diffraction pattern in Fig. 5b. VO_2 exhibits two distinctive domains (grains showing the same orientation are considered as one domain). The corresponding diffraction patterns are shown in Fig. 5c and d. The (0006) diffraction disk in sapphire is close to the $(0\bar{2}0)$

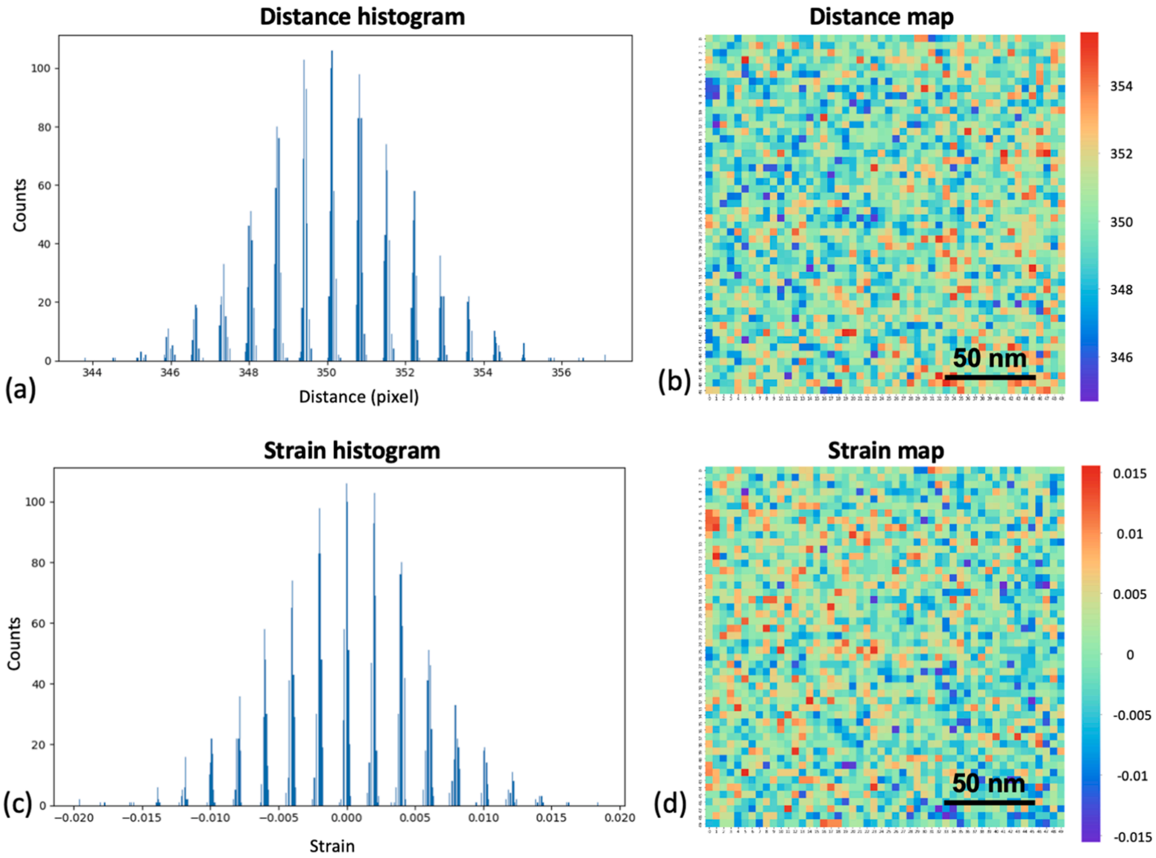

Fig. 4. (a) Distance histogram and (b) distance map of a pristine single crystal sapphire specimen. The corresponding (c) strain histogram and (d) strain map generated using the $(\bar{2}024)$ and $(20\bar{2}\bar{4})$ reflections (white circles in Fig. 3b).

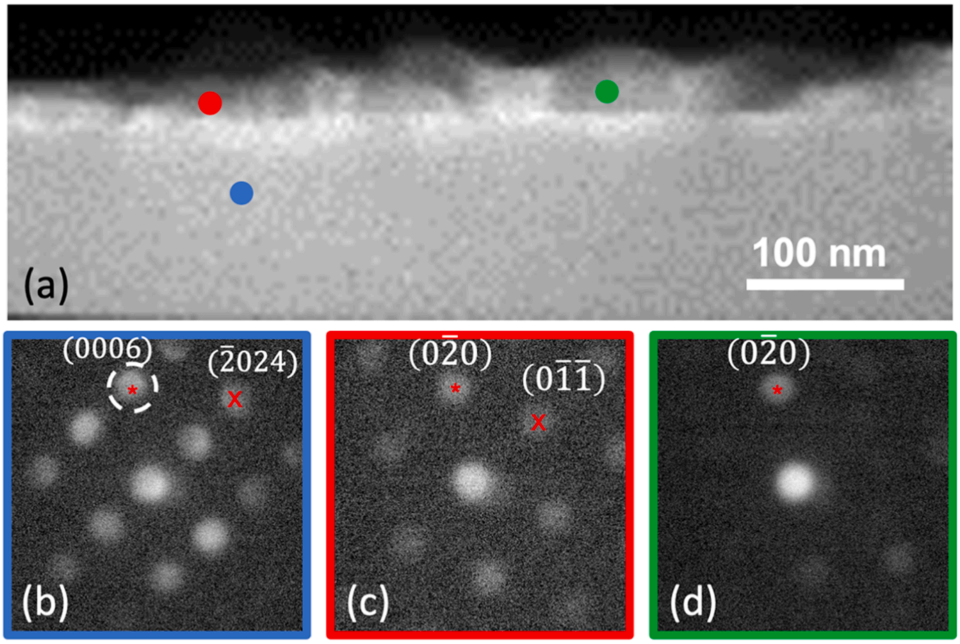

Fig. 5. (a) Virtual dark-field image of VO_2 film on the sapphire substrate. The diffraction patterns of sapphire and two domains of VO_2 are shown in (b), (c), and (d), respectively. The virtual dark-field image was reconstructed using (0006) reflection (highlighted with the dashed circle). Common/similar diffraction disks in sapphire and VO_2 are indicated by "*" and "X".

diffraction disk in both domains in VO_2 (marked by "*" in Fig. 5b-d). The $(\bar{2}024)$ diffraction disk in sapphire is close to the $(0\bar{1}\bar{1})$ diffraction disk one of the VO_2 domains (marked by "X" in Fig. 5b,c).

Fig. 6 shows the strain maps with the corresponding selected diffraction disks (highlighted by the white circles) and the distance

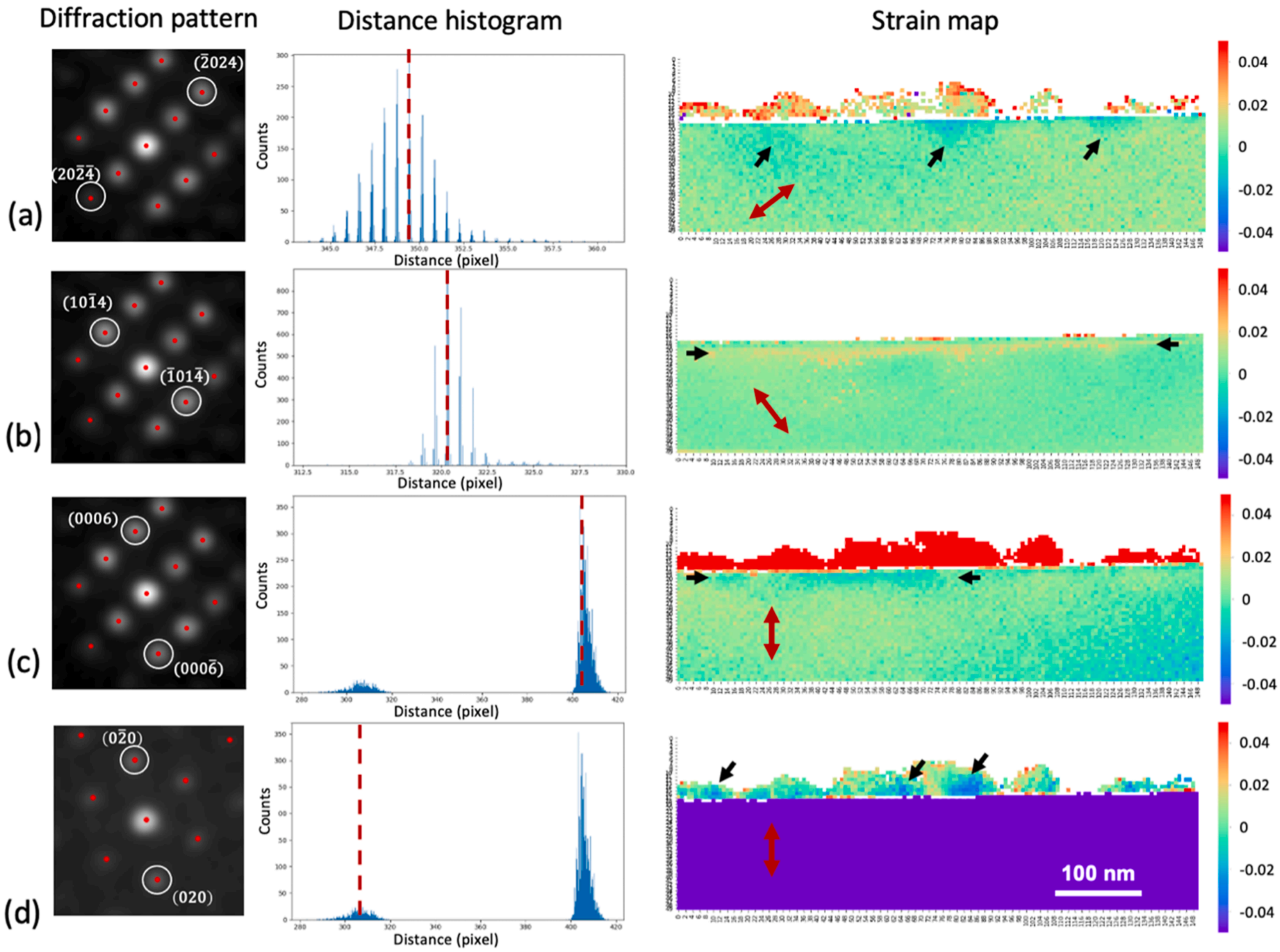

Fig. 6. Selected diffraction disk for strain mapping, distance histogram, and corresponding strain maps using (a) $(\bar{2}024)$ and $(20\bar{2}\bar{4})$ reflections in sapphire and $(0\bar{1}\bar{1})$ (011) reflections in VO_2, (b) $(10\bar{1}4)$ and $(\bar{1}01\bar{4})$ reflections in sapphire, (c) (0006) and $(000\bar{6})$ reflections in sapphire, and (d) $(0\bar{2}22)$ and (020) reflections in VO_2 shown in Fig. 5. Red dashed lines indicate where the reference distances were taken from. Black arrows highlight the strained regions. Red double arrows indicate the strain direction. Note that the red film in (c) and violet substrate in (d) are artifacts. (For interpretation of the references to color in this figure legend, the reader is referred to the web version of this article.).

histograms. The strain direction is marked by the red double arrows in the strain maps, which is the ***g***-vector direction of the selected diffraction disks after the magnetic rotation correction in diffraction patterns. In the first case, the $(20\bar{2}\bar{4})$ and $(\bar{2}024)$ diffraction disks in sapphire (and the (011) and $(0\bar{1}\bar{1})$ diffraction disks in VO_2 of one of the domains due to proximity) were selected (Fig. 6a). Note that the distance distribution is skewed because of the interplanar spacing differences between sapphire and VO_2 and the non-symmetric strain distribution in the sapphire substrate. Determining the strain-free distance is not as direct as the single crystal sapphire case in Fig. 4. Considering the sapphire substrate is largely unstrained, we treated the mode of the dataset (indicated by the red dashed line in the distance histogram) as the reference distance. Pockets of compressive strained regions (approximately -1.5%) near the interface (indicated by the black arrows) were observed in sapphire. It is also important to point out that the strain in the VO_2 film in Fig. 6a is relative because the sapphire was selected as the reference. Nonetheless, semi-quantitative strain distribution information was demonstrated. A similar approach was adopted to analyze the strain distribution in sapphire of the $(10\bar{1}4)$ planes (Fig. 6b). It is apparent a narrow tensile-strained region (approximately 2.5%, indicated by the black arrows) was revealed beneath the interface.

The interplanar spacing values of (0006) in sapphire and $(0\bar{2}0)$ in VO_2 are 2.17 A and 2.74 A, respectively. These values are different enough to give rise to two distinct peaks in the distance histogram. When focusing on sapphire (Fig. 6c), the reference distance was the mode from only the substrate. A narrow region of compressive strain (approximately -2%) was observed below part of the interface (indicated by the black arrows). When focusing on the VO_2 (Fig. 6d), the reference distance was the median from only the film, and regions of compressive strain (approximately -3%) were noted (indicated by the black arrows). The film appears red in Fig. 6c and the substrate violet in Fig. 6d, which are artifacts caused by intermixing the VO_2 and sapphire information in the strain analysis.

3.4. Case study 2: Strain in martensite plates of a $Ni_{50.3}Ti_{29.7}Hf_{20}$ SMA

To further demonstrate the wide application of this method to map residual strains, a $Ni_{50.3}Ti_{29.7}Hf_{20}$ SMA sample was selected as a model system. The NiTiHf SMAs undergo B2 austenite to B19' martensite phase transformation when they are cooled below their phase transformation temperatures. It is well known that large elastic strain can be stored in the martensite but there is limited understanding of the stored strains in martensite. Elastic strain is particularly important in martensitic transformation. This is because, unlike the diffusional transformation that nucleation occurs at interfaces, martensitic nucleation takes placed in the elastically strained regions [45]. In turn, the stored strain in martensite may promote or hinder martensite-to-austenite phase transformation. Hence, it is imperative understand the residual strain in these systems.

This case study demonstrates an example of how our algorithm can reveal the residual strain in martensite grains even when the crystals are not tilted to zone axes. The scanned area contains two martensite plates and the virtual bright-field image reconstructed by the intensity of the direct beam is shown Fig. 7a. No tilting in TEM was performed, so the orientations of the crystals are rather random. The top martensite variant happens to be in a two-beam condition and the bottom one close to a two-beam condition, as shown in the diffraction patterns in Fig. 7b, c. Note that the distortion matrix method cannot be applied to this type of datasets to resolve residual strain. Using our algorithm, the diffraction disks for generating strain maps are highlighted by the white circles. In each martensite variant, since the distance histogram shows a normal distribution, the mean of the distance values was considered as the reference. The distance histograms and the strain maps of the martensite variants are displayed in Fig. 8. The red double arrow indicates the strain direction. For the top martensite (Fig. 8a), the residual strain is largely compressive (approximately -3%) near the grain boundary. For the bottom martensite (Fig. 8b), the area near the grain boundary is slightly compressive (approximately -1%), and the strain distribution 200 nm away from the grain boundary is complex, with areas of compressive and tensile strain intermixing together. (The violet region in Fig. 8a and red region in Fig. 8b are artifacts, similar to those in Fig. 6c,d). The strain mapping results demonstrated here can be combined with *in situ* heating experiment to explore the effect of strain type and magnitude on the martensitic transformation, which will be a subject of future studies.

3.5. Advantages, disadvantages, and concerns of this algorithm

Our newly developed strain mapping algorithm has some unique advantages compared to the other available algorithms. The first advantage is that our algorithm does not require the user to select a “strain-free” area in the map as the reference pattern. Reference areas can be easily identified in device materials (e.g., silicon substrate far away from the interface). However, such areas are challenging to identify in structural materials (especially for those have undergone complex thermomechanical treatments) and nanocrystalline thin films (such as the VO_2 thin film in *Case Study 1*). In our approach, the reference is obtained by analyzing the distance data, either by taking the mean or the mode of the dataset, which eliminates the need to locate a reference area in the specimen. The second advantage is that our algorithm can work on crystals not at zone axes, in contrast to the distortion matrix approach [29]. In the distortion matrix approach, two non-colinear vectors are created, which requires 2D-symmetry of the diffraction pattern (i.e., at a zone axis). In our method, we only compare the distance between the selected disks, which also works on diffraction patterns that are not at zone axes, as demonstrated in one of the VO_2 domains and SMA martensite examples. The third advantage is that the distance histogram obtained from our algorithm is analogous to the peaks in x-ray diffractograms (XRD). Both exhibit data in reciprocal space. The symmetry and width of the peak in the distance histogram bear statistical lattice spacing and strain information of the mapped area, which is not available from other algorithms. Moreover, techniques that extract information from XRD peaks (e.g., estimating dislocation density [46]) may also be applied to the distance histogram to generate quantitative microstructural information.

The user may be concerned with some potential disadvantages of our strain mapping method. First, our method has relatively poor strain resolution (~1%) compared to the current distortion matrix algorithms in PED (0.03%–0.05%) [21,32] and 4D-STEM (0.1%) [19] reported in the literature. We had a closer inspection of outlier pixels (e.g., pixels outside 2-sigma in Fig. 4) usually exhibit skewed intensity distribution in the selected diffraction disks. Better filter and disk/spot identification algorithms can be incorporated in the future to further improve the strain resolution of our approach. We then further compared the strain maps of the VO_2 thin film on sapphire substrate created by the commercial PED-STRAIN software (Fig. 9a) and our algorithm (Fig. 9b). The strain maps were generated using the $(20\overline{24})$ and $(\bar{2}024)$ diffraction disks in sapphire (similar to the example shown in Fig. 6a), and three compressively strained regions were revealed in both maps (highlighted by the black arrow). To our pleasure, two strain maps show good agreement, suggesting our algorithm a powerful tool to identify residual strains in materials at the nano-scale with comparable accuracy to the commercial software, although it seems to have a lower strain resolution. Note that the absolute strain values calculated by the commercial software and our algorithm are not directly comparable due to the different “strain-free” references. Second, our approach can only generate the normal strain components, whereas the distortion matrix method can also calculate the shear and rotational components. This is an intrinsic limitation of our algorithm. We gave up the distortion matrix approach to enable strain mapping using diffraction patterns not at zone axis (e.g., at two-beam conditions). Unfortunately, the improved

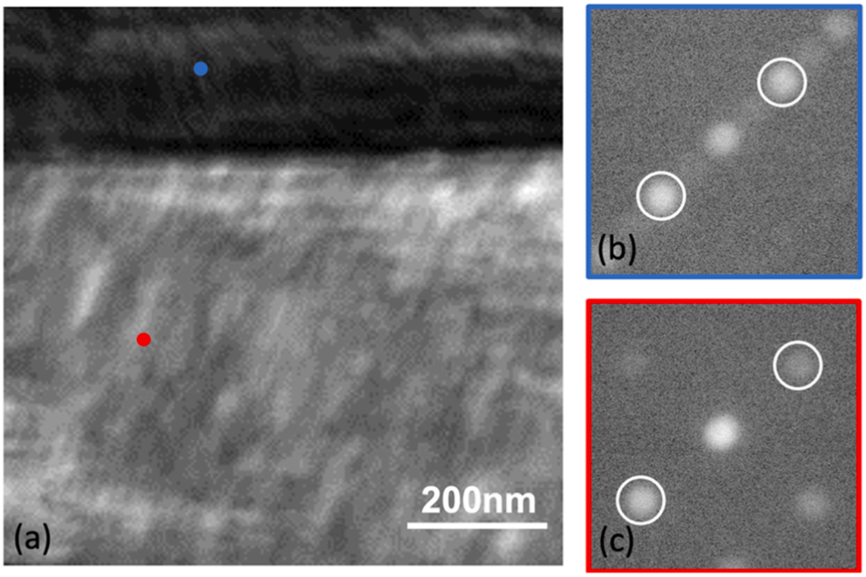

Fig. 7. (a) Virtual bright-field image of two martensite variants in the $Ni_{50.3}Ti_{29.7}Hf_{20}$ SMA. Diffraction patterns of (b) the top variant and (c) the bottom variant. The diffracted disks used for strain calculation are highlighted with white circles.

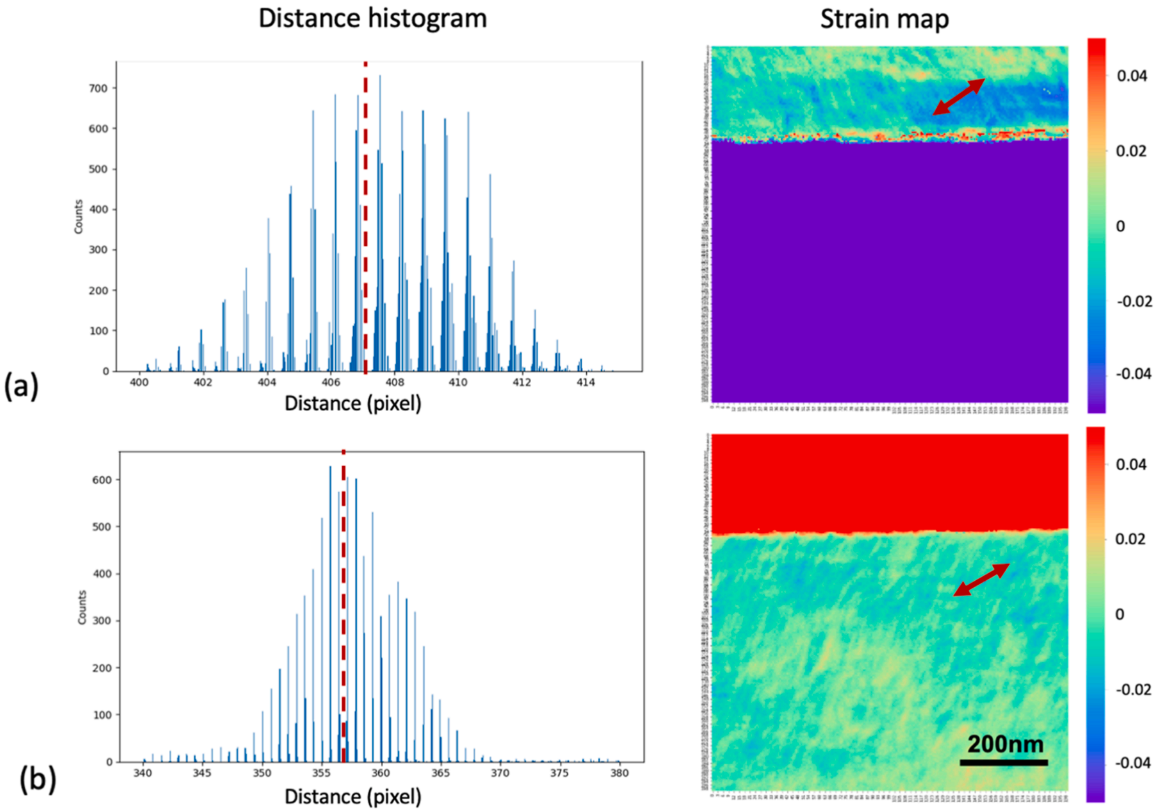

Fig. 8. Distance histogram and strain map of (a) the top martensite variant and (b) the bottom martensite variant shown in Fig. 7. Red dashed lines indicate the reference distance used in strain mapping. Red arrows refer to the strain directions. Note the violet top martensite in (a), and red bottom martensite in (b) are artifacts. (For interpretation of the references to color in this figure legend, the reader is referred to the web version of this article.).

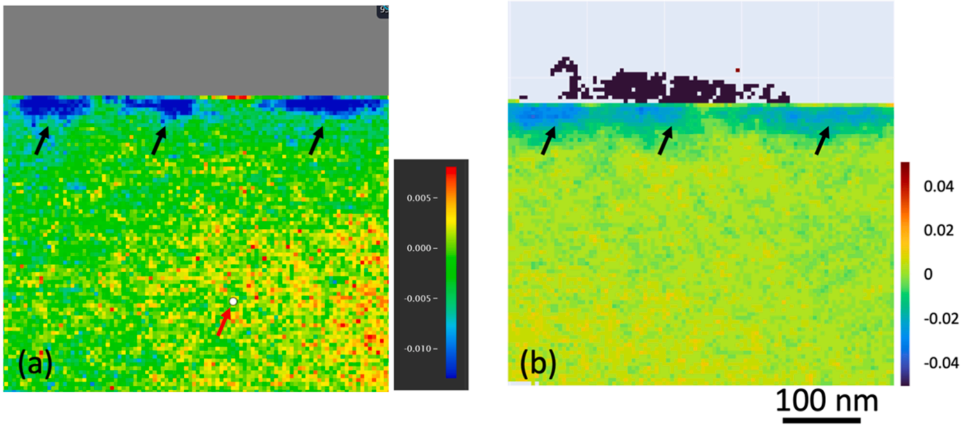

Fig. 9. Strain maps from part of a sapphire substrate (containing the sapphire-VO_2 interface) obtained from (a) the PED-strain commercial software and (b) our algorithm, showing good agreement. Black arrows highlight the strained regions. The Red arrow in (a) points to a white dot, which was manually selected by the user as a “strain-free” reference. The dark navy film on top in (b) is an artifact. (For interpretation of the references to color in this figure legend, the reader is referred to the web version of this article.).

versatility is at the cost of sacrificing other strain information.

It is also worth discussing whether the strain calculation using our method can be affected by the diffraction spot shift when the sample is not at a zone axis. When a TEM specimen is tilted at a zone axis, the Ewald sphere intersects with the centers of the relrods [16]. When a TEM specimen is tilted off the zone axis, an excitation error occurs. In this diffraction condition, the measured distance between the center beam and the diffracted beam (as well as between the selected disks) will be different from that when the same crystal is tilted to a zone axis, which may potentially lead to strain measurement discrepancy. Therefore, the strains measured from different grains using the same diffraction disk may not be directly compared. However, strain within the same grain or the same domain, even when it is off zone axes, can be compared because the excitation error is consistent in such a grain.

4. Conclusions

In summary, a new reference-area-free approach for strain mapping was developed to analyze PED data. Different image filters were used to first denoise the diffraction patterns. Template matching using the direct beam was then employed to identify the positions of diffraction disks. Statistics of distances between the selected diffracted disks enable the user to make an informed decision on the reference and to generate strain maps. With this method, we were able to successfully measure and map the residual elastic strain in VO_2 on sapphire and for the $Ni_{50.3}Ti_{29.7}Hf_{20}$ martensite. This approach does not require the user to select a “strain-free” area as a reference and can work on datasets even with the crystals oriented away from zone axes. We expect this method to provide a more accessible alternative to CBED and nano-beam electron diffraction (NBED) of studying residual strain of various material systems that complements the existing algorithms for strain mapping at the nano-scale.

Declaration of Competing Interest

The authors declare that they have no known competing financial interests or personal relationships that could have appeared to influence the work reported in this paper.

Data availability

Data will be made available on request.

Acknowledgments

D.Z. and K.X. acknowledge the funding support from the X-Grant at TEES. A.P., A.B., M.H., A.W., J.D., T.U., I.K., and K.X. acknowledge the funding support from the National Science Foundation (NSF-DMR, grant number: 2004752). Y.Z., P.S., S.B., and M.P. acknowledge partial support from the Department of Energy under DE-SC0023353. The authors also would like to acknowledge the instrument and technical support from the Microscopy & Imaging Center (MIC) at Texas A&M University. The code of our algorithm can be found on Github https://github.com/TAMU-Xie-Group/PED-Strain-Mapping. The tutorial on how to use our code can be found on YouTube https://www.youtube.com/playlist?list=PLzldQixzgawCiatAjgMeHAzG-c6JdX1V6.

References

[1] J.B. Wachtman, W.R. Cannon, M.J. Matthewson, Mechanical Properties of Ceramics, John Wiley & Sons, 2009.

[2] R.W. Hertzberg, R.P. Vinci, J.L. Hertzberg, Deformation and Fracture Mechanics of Engineering Materials, John Wiley & Sons, 2020.

[3] K.F. Murphy, B. Piccione, M.B. Zanjani, J.R. Lukes, D.S. Gianola, Strain-and defect-mediated thermal conductivity in silicon nanowires, Nano Lett. 14 (2014) 3785–3792.

[4] B. Piccione, D.S. Gianola, Tunable thermoelectric transport in nanomeshes via elastic strain engineering, Appl. Phys. Lett. 106 (2015), 113101.

[5] J. Qi, X. Qian, L. Qi, J. Feng, D. Shi, J. Li, Strain-engineering of band gaps in piezoelectric boron nitride nanoribbons, Nano Lett. 12 (2012) 1224–1228.

[6] M.E. Fitzpatrick, A. Lodini, Analysis of Residual Stress By Diffraction Using Neutron and Synchrotron Radiation, CRC Press, 2003.

[7] P. Withers, M. Turski, L. Edwards, P. Bouchard, D. Buttle, Recent advances in residual stress measurement, Int. J. Press. Vessels Piping 85 (2008) 118–127.

[8] D. Cooper, T. Denneulin, N. Bernier, A. Béché, J.-L. Rouviere, Strain mapping of semiconductor specimens with nm-scale resolution in a transmission electron microscope, Micron 80 (2016) 145–165.

[9] A. Béché, J. Rouvière, J. Barnes, D. Cooper, Strain measurement at the nanoscale: comparison between convergent beam electron diffraction, nano-beam electron diffraction, high resolution imaging and dark field electron holography, Ultramicroscopy 131 (2013) 10–23.

[10] M. Hÿtch, E. Snoeck, R. Kilaas, Quantitative measurement of displacement and strain fields from HREM micrographs, Ultramicroscopy 74 (1998) 131–146.

[11] J.-L. Rouviere, E. Sarigiannidou, Theoretical discussions on the geometrical phase analysis, Ultramicroscopy 106 (2005) 1–17.

[12] J. Zuo, J. Spence, Automated structure factor refinement from convergent-beam patterns, Ultramicroscopy 35 (1991) 185–196.

[13] J.M. Zuo, J.C. Spence, Strain measurements and mapping, in: Advanced Transmission Electron Microscopy, Springer, 2017, pp. 553–580.

[14] V. Randle, I. Barker, B. Ralph, Measurement of lattice parameter and strain using convergent beam electron diffraction, J. Electron. Microsc. Tech. 13 (1989) 51–65.

[15] L. Clément, R. Pantel, L.T. Kwakman, J. Rouvière, Strain measurements by convergent-beam electron diffraction: the importance of stress relaxation in lamella preparations, Appl. Phys. Lett. 85 (2004) 651–653.

[16] D.B. Williams, C.B. Carter, Transmission Electron Microscopy: Diffraction, Springer, 2009.

[17] C. Deininger, G. Necker, J. Mayer, Determination of structure factors, lattice strains and accelerating voltage by energy-filtered convergent beam electron diffraction, Ultramicroscopy 54 (1994) 15–30.

[18] C. Ophus, Four-dimensional scanning transmission electron microscopy (4D-STEM): from scanning nanodiffraction to ptychography and beyond, Microsc. Microanal. 25 (2019) 563–582.

[19] V. Ozdol, C. Gammer, X. Jin, P. Ercius, C. Ophus, J. Ciston, A. Minor, Strain mapping at nanometer resolution using advanced nano-beam electron diffraction, Appl. Phys. Lett. 106 (2015), 253107.

[20] P.A. Midgley, A.S. Eggeman, Precession electron diffraction–a topical review, IUCrJ 2 (2015) 126–136.

[21] M. Vigouroux, V. Delaye, N. Bernier, R. Cipro, D. Lafond, G. Audoit, T. Baron, J. Rouvière, M. Martin, B. Chenevier, Strain mapping at the nanoscale using precession electron diffraction in transmission electron microscope with off axis camera, Appl. Phys. Lett. 105 (2014), 191906.

[22] R. Vincent, P. Midgley, Double conical beam-rocking system for measurement of integrated electron diffraction intensities, Ultramicroscopy 53 (1994) 271–282.

[23] P. Oleynikov, S. Hovmöller, X. Zou, Precession electron diffraction: observed and calculated intensities, Ultramicroscopy 107 (2007) 523–533.

[24] T.C. Pekin, C. Gammer, J. Ciston, A.M. Minor, C. Ophus, Optimizing disk registration algorithms for nanobeam electron diffraction strain mapping, Ultramicroscopy 176 (2017) 170–176.

[25] S.E. Zeltmann, A. Müller, K.C. Bustillo, B. Savitzky, L. Hughes, A.M. Minor, C. Ophus, Patterned probes for high precision 4D-STEM bragg measurements, Ultramicroscopy 209 (2020), 112890.

[26] E. Padgett, M.E. Holtz, P. Cueva, Y.-T. Shao, E. Langenberg, D.G. Schlom, D. A. Muller, The exit-wave power-cepstrum transform for scanning nanobeam electron diffraction: robust strain mapping at subnanometer resolution and subpicometer precision, Ultramicroscopy 214 (2020), 112994.

[27] C. Mahr, K. Müller-Caspary, T. Grieb, F.F. Krause, M. Schowalter, A. Rosenauer, Accurate measurement of strain at interfaces in 4D-STEM: a comparison of various methods, Ultramicroscopy 221 (2021), 113196.

[28] R. Yuan, J. Zhang, L. He, J.-M. Zuo, Training artificial neural networks for precision orientation and strain mapping using 4D electron diffraction datasets, Ultramicroscopy 231 (2021), 113256.

[29] J.-L. Rouviere, A. Béché, Y. Martin, T. Denneulin, D. Cooper, Improved strain precision with high spatial resolution using nanobeam precession electron diffraction, Appl. Phys. Lett. 103 (2013), 241913.

[30] B.H. Savitzky, S.E. Zeltmann, L.A. Hughes, H.G. Brown, S. Zhao, P.M. Pelz, T. C. Pekin, E.S. Barnard, J. Donohue, L.R. DaCosta, py4DSTEM: a software package for four-dimensional scanning transmission electron microscopy data analysis, Microsc. Microanal. 27 (2021) 712–743.

[31] A. Darbal, R. Narayan, C. Vartuli, T. Aoki, J. Mardinly, S. Nicolopoulos, J. Weiss, Applications of automated high resolution strain mapping in TEM on the study of strain distribution in MOSFETs, Microsc. Microanal. 20 (2014) 1066–1067.

[32] P.F. Rottmann, K.J. Hemker, Nanoscale elastic strain mapping of polycrystalline materials, Mater. Res. Lett. 6 (2018) 249–254.

[33] L. Ma, P.F. Rottmann, K. Xie, K.J. Hemker, Nano-scale elastic strain maps of twins in magnesium alloys, Microsc. Microanal. 24 (2018) 970–971.

[34] Y. Yang, R. Zhang, S. Zhao, Y. Deng, Q. Yu, S. Zeltmann, S. Yin, J. Ciston, C. Ophus, M. Asta, In situ observations and measurements of plastic deformation, phase transformations and fracture with 4D-STEM, Microsc. Microanal. 27 (2021) 1494–1495.

[35] R. Yuan, J. Zhang, J.-M. Zuo, Lattice strain mapping using circular Hough transform for electron diffraction disk detection, Ultramicroscopy 207 (2019), 112837.

[36] A. Béché, J. Rouvière, L. Clément, J. Hartmann, Improved precision in strain measurement using nanobeam electron diffraction, Appl. Phys. Lett. 95 (2009), 123114.

[37] S. Wang, T.B. Eldred, J.G. Smith, W. Gao, AutoDisk: automated diffraction processing and strain mapping in 4D-STEM, Ultramicroscopy 236 (2022), 113513.

[38] J. Jian, X. Wang, L. Li, M. Fan, W. Zhang, J. Huang, Z. Qi, H. Wang, Continuous tuning of phase transition temperature in VO2 thin films on c-cut sapphire substrates via strain variation, ACS Appl. Mater. Interfaces 9 (2017) 5319–5327.

[39] G. Bigelow, A. Garg, S. Padula Ii, D. Gaydosh, R. Noebe, Load-biased shape-memory and superelastic properties of a precipitation strengthened high-temperature Ni50. 3Ti29. 7Hf20 alloy, Scr. Mater. 64 (2011) 725–728.

[40] J. Dong, T. Umale, B. Young, I. Karaman, K.Y. Xie, Structure and substructure characterization of solution-treated Ni50. 3Ti29. 7Hf20 high-temperature shape memory alloy, Scr. Mater. 219 (2022), 114888.

[41] F. de la Peña, T. Ostasevicius, V.T. Fauske, P. Burdet, P. Jokubauskas, M. Nord, M. Sarahan, E. Prestat, D.N. Johnstone, J. Taillon, Electron microscopy (big and small) data analysis with the open source software package HyperSpy, Microsc. Microanal. 23 (2017) 214–215.

[42] R.C. Gonzalez, Digital Image Processing, Pearson Education India, 2009.

[43] K. Müller, A. Rosenauer, M. Schowalter, J. Zweck, R. Fritz, K. Volz, Strain measurement in semiconductor heterostructures by scanning transmission electron microscopy, Microsc. Microanal. 18 (2012) 995–1009.

[44] M. Nord, J. Verbeeck, Open source development tools for robust and reproducible electron microscopy data analysis, Microsc. Microanal. 25 (2019) 138–139.

[45] G. Olson, M. Cohen, A mechanism for the strain-induced nucleation of martensitic transformations, J. Less Common Metals 28 (1972) 107–118.

[46] P. Gay, P. Hirsch, A. Kelly, The estimation of dislocation densities in metals from X-ray data, Acta Metallurgica 1 (1953) 315–319.